UCRL-16846

# University of California

# Ernest O. Lawrence Radiation Laboratory

CALCULATION AND MEASUREMENT OF THE YIELD STRESS OF ALLOYS WITH COHERENT LAMELLAR MICROSTRUCTURES

TWO-WEEK LOAN COPY

*This is a Library Circulating Copy which may be borrowed for two weeks. For a personal retention copy, call Tech. Info. Division, Ext. 5545*

## DISCLAIMER

This document was prepared as an account of work sponsored by the United States Government. While this document is believed to contain correct information, neither the United States Government nor any agency thereof, nor the Regents of the University of California, nor any of their employees, makes any warranty, express or implied, or assumes any legal responsibility for the accuracy, completeness, or usefulness of any information, apparatus, product, or process disclosed, or represents that its use would not infringe privately owned rights. Reference herein to any specific commercial product, process, or service by its trade name, trademark, manufacturer, or otherwise, does not necessarily constitute or imply its endorsement, recommendation, or favoring by the United States Government or any agency thereof, or the Regents of the University of California. The views and opinions of authors expressed herein do not necessarily state or reflect those of the United States Government or any agency thereof or the Regents of the University of California.

Special thesis

UCRL-16846

UNIVERSITY OF CALIFORNIA

Lawrence Radiation Laboratory
Berkeley, California

AEC Contract W-7405-eng-48

# CALCULATION AND MEASUREMENT OF THE YIELD STRESS OF ALLOYS WITH COHERENT LAMELLAR MICROSTRUCTURES

Shelley Dean Dahlgren

May 1966

(Ph.D. Thesis)

# CALCULATION AND MEASUREMENT OF THE YIELD STRESS OF ALLOYS WITH COHERENT LAMELLAR MICROSTRUCTURES

Shelley Dean Dahlgren

Inorganic Materials Research Division, Lawrence Radiation Laboratory,
Department of Mineral Technology, College of Engineering,
University of California, Berkeley, California

May 1966

ABSTRACT

Coherency strain fields in precipitation hardened alloys are usually non-uniform and difficult to analyze. Cu-Ni-Fe alloys, however, can be made to possess coherent lamellar microstructures which have small and uniform strains. Calculations of yield stresses based on these coherency strains agree well with measured values. The yield stresses of the Cu-Ni-Fe alloys studied are independent of the interlamellar spacing and independent of the volume fractions of the two chemically different lamellae present; however, they are directly proportional to the differences in cubic lattice parameters of the two kinds of plates forming the lamellar structure.

The lamellar microstructures are produced from supersaturated solid solutions by a demixing process. That is, atoms of one kind cluster to form one type of lamellae and the remaining atoms cluster to form the other type of lamellae which form during low temperature transformation. Because the average atom sizes are different in the two chemically different lamellae the lamellar plates must be strained in order for coherency to be maintained between the lamellae. On overaging this coherency is lost and the compositions of the two lamellae are given by the positions of the phase boundary lines on the equilibrium diagram. However, when coherency is maintained, it is shown in the present work that the demixing process is stopped short of completion at low tem-

TABLE OF CONTENTS


I. Introduction ..... 1

II. Theory ..... 5

III. Experimental Procedure ..... 22

IV. Experimental Results ..... 24

V. Discussion of Results ..... 25

VI. Conclusions ..... 35

Acknowledgements ..... 36

References ..... 37

Figure Captions ..... 39

Tables ..... 40

Figures ..... 43

# I. INTRODUCTION

Soon after age hardening alloys were discovered, it was suggested that internal coherency strains were important contributors to the amazing strength increases obtained during aging. In recent years theories have been advanced to quantitatively assess these strains but this has been a difficult task because of the complex nature of the strain fields near precipitate particles.

It was the objective of this study to select an alloy system in which the strains were small and the strain fields relatively uniform in both the matrix and a coherent precipitate in order to calculate the internal strains and relate these strains to the yield stress of the alloy. Alloys with the desired characteristics were found in the ternary system Cu-Ni-Fe.

The copper-nickel-iron system has been thoroughly investigated both from the phase diagram aspect[1,2] and from the structural standpoint.[3-10] The isothermal section of the Cu-Ni-Fe phase diagram for 600°C is reproduced in Fig. 1, and it includes the tie lines for that temperature. A vertical section constructed from several isothermal sections and passing along any tie line would reveal a pseudo-binary diagram with a large miscibility gap. These alloys show the well-known spinodal transformation. The volume fractions and the difference in the lattice parameters of the two "phases"* formed during precipitation can be varied over a wide range through

---

* Although it is recognized that non-equilibrium, pre-precipitation segregated regions are not phases in the rigorous sense of the word, the term is used herein for convenience of discussion.

composition and aging temperature variations.

Before the equilibrium FCC phases finally form, two intermediate decomposition stages are encountered during low temperature aging of samples quenched from above the miscibility gap. The first stage is called the "side-band" state because of the satellite reflections which appear on either side of the main reflections in Debye-Sherrer x-ray patterns. These satellites are due to one-dimensional composition (and therefore lattice parameter) fluctuations in face-centered-cubic material. The satellite position with respect to the main Bragg line is a function of the wavelength of the composition fluctuation and is more removed from the main line the smaller the wavelength.[4] A sine wave[4] has been used to approximate the composition-distance curve, although others[7,11] have suggested that a square or more general wave shape would be just as appropriate. No method has been devised to ascertain experimentally the exact wave form that exists during the transformation.

The second stage x-ray patterns reveal the formation of two tetragonal structures.[3,7,8] The two non-equilibrium structures have a common "a" tetragonal lattice parameter which is constant throughout both structures. One of these structures has a c/a ratio less than one while the other has a c/a ratio greater than unity. The morphology of the two phases is lamellar with the plates lying parallel to {100} planes. The two tetragonal "a" axes lie in the common {100} plane and the "c" axes are normal to this plane.[3,4] It is apparent that the second stage structure also possesses a one-dimensional lattice parameter variation along the "c" axis which probably more nearly approaches a square wave configuration than is the case during the earlier "side band" state. Because the fluctuation wavelength of the tetragonal state is larger than that of the

"side-band" state, the difference in stages one and two may be only one of degree. Bagaryatskii and Tyapkin[12,13] have shown in similar transformations found in Ni-Ti and Ni-Cr-Ti alloys that the two stages described above are observed with soft x-radiation but only one stage is found with hard radiation. This supports the suggestion that the appearance of two different intermediate structures during aging is only a matter of degree in a continuously changing system. (Kelly and Nicholson[14] have reviewed the work of Bagaryatskii and Tyapkin and other work pertinent to the present investigation.)

The microstructure of greatest interest is the one which gives the maximum room temperature yield stress for any given aging temperature. This maximum occurs at a time when the magnetic coercivity and other properties[8] are at a maximum and when the transformation is still in the "side-band" stage. Errors in determining the maximum yield point as a function of aging time were not found to be critical because the maximum is very broad in Cu-Ni-Fe alloys (e.g. see Fig. 5).

The "side-band" microstructure can be considered as two tetragonal structures with $c/a < 1$ and $c/a > 1$ where a is constant and c is a function of position. Thus a one dimensional lattice parameter fluctuation occurs. The basic assumption employed in the theory to be developed is that the tetragonality of the two structures is caused by elastic strains needed to maintain coherency of two structures that, if unattached, would be cubic. It has been shown[2] that all compositions of precipitating phases in Cu-Ni-Fe alloys are cubic when quenched from above the miscibility gap and they are cubic when overaging has caused a loss of coherency.[7] One of the phases has a cubic parameter that is too small to match with the

other and consequently plates of this phase will be stressed in two dimensional tension in the coherent state. Likewise plates of the other phase will be stressed in compression. It has been suggested[15] that these coherency strains inhibit the transformation such that the phase compositions do not reach those given by the equilibrium diagram until coherency is lost. The end effects introduce a complication in the stress analysis, but because the plates are long compared to their thickness, as indicated by the electron micrograph of Fig. 2, the end effects can be neglected.

## II. THEORY

The method to be followed in calculating the yield stress of lamellar alloys is to determine the magnitude of the stresses which are present in the microconstituents of the alloys and to resolve these stresses along the slip plane in order to relate them to the first large migration of dislocations enforced by a gradually increasing load. In the analysis, a square wave composition-distance curve will first be assumed. The resulting structure will then be as shown in Fig. 3. The subscripts 1 and 2 refer respectively to the properties of the phase with $c_1/a < 1$ and to the phase with $c_2/a > 1$. Let $\bar{a}$ represent the common non-equilibrium "a" parameter of the two tetragonal phases, and let $a_{10}$ and $a_{20}$ be the equilibrium cubic lattice parameters for the most extreme compositions existing in the plates. These two values will tend to approach those of the equilibrium phases.

The cross-hatched plane of Fig. 3 represents a cut section through the lamella and the external forces $F_{x1}$ and $F_{x2}$ replace the constraints which were present before the cut; $\lambda$ is the wavelength of the composition fluctuation and $f_1$ and $f_2 = (1-f_1)$ are the volume fractions of the two phases. Since $c_1 < \bar{a}$ and $c_2 > \bar{a}$ the total displacement over many lamella in the z direction will be small and therefore the assumption $\sigma_z = 0$, where $\sigma_z$ is the stress in the z direction, is made. The effect of having $\sigma_z$ differ from zero is to raise the stresses in plates of one composition while it lowers the stresses in the plates of the other composition by a corresponding amount. The net effect eventually nearly cancels when the final calculations are made (cf. Eq. (26)).

From $\Sigma F_x = 0$ and Fig. 3 it can be seen that

$$\sigma_{x1} L\lambda f_1 = -\sigma_{x2} L\lambda f_2 \tag{1}$$

($\sigma_{x2}$ will have a negative sign showing compression since plus x is taken to be the positive direction of stress.) Because the phases are known to be tetragonal and are not orthorhombic, $\sigma_x = \sigma_y$ in both phases. $\sigma_{x1}$ and $\sigma_{x2}$ are constants when a square wave composition-distance curve is assumed.

Equation (1) can also be obtained for a more general composition-distance wave form. For this case let $\sigma_{x1}$ vary across plates of composition 1 according to the expression.

$$\sigma_{x1} = \sigma_{x1}\Big|_{max} \sum_{1}^{n} A_{1n} \sin \frac{2\pi nz}{\lambda_1}, \quad (0 \leq z \leq \frac{\lambda_1}{2}) \tag{2}$$

where the maximum amplitude of $\sum_{1}^{n} An \sin \frac{2\pi nz}{\lambda_1}$ is restricted to unity. Therefore $\sigma_{x1} \leq \sigma_{x1}\Big|_{max}$ where $\sigma_{x1}\Big|_{max}$ is a constant. Also in plates of composition 2

$$\sigma_{x2} = \sigma_{x2}\Big|_{max} \sum_{1}^{n} A_{2n} \sin \frac{2\pi nz}{\lambda_2}, \left( \frac{\lambda_2}{2} \leq z \leq \lambda_2 \right)$$

or

$$\sigma_{x2} = -\sigma_{x2}\Big|_{max} \sum_{1}^{n} A_{2n} \sin \frac{2\pi nz'}{\lambda_2}, \left( 0 \leq z' \leq \frac{\lambda_2}{2} \right) \tag{3}$$

where $z' = z - \frac{\lambda_2}{2}$ and $|\sigma_{x2}| \leq \sigma_{x2}\Big|_{max}$ where $\sigma_{x2}\Big|_{max}$ is a positive constant and $\sigma_{x2}$ is a compressive stress, i.e., $\sigma_{x2} < 0$. $\lambda_1$ and $\lambda_2$ are related to the modulation wavelength by

$$\frac{\lambda_1}{2} + \frac{\lambda_2}{2} = \lambda$$

and the volume fractions $f_1$ and $f_2$ are related to $\lambda_1$ and $\lambda_2$ by

$$\frac{f_1}{f_2} = \frac{\lambda_1}{\lambda_2} . \tag{4}$$

Again, $\Sigma F_x = 0$ and

$$L \int_0^{\frac{\lambda_1}{2}} \sigma_{x1}\Big|_{max} \sum_1^n A_{1n} \sin \frac{2\pi mz}{\lambda_1} dz = -L \int_0^{\frac{\lambda_2}{2}} -\sigma_{x2}\Big|_{max} \sum_1^n A_{2n} \sin \frac{2\pi mz'}{\lambda_2} dz' . \tag{5}$$

On integrating both sides of the equation between the given limits

$$-\sigma_{x1}\Big|_{max} \frac{\lambda_1}{2\pi} \left\{ \sum_1^n \left( \frac{A_{1n}}{n} \cos \pi n + \frac{A_{1n}}{n} \right) \right\} = -\sigma_{x2}\Big|_{max} \frac{\lambda_2}{2\pi} \left\{ \sum_1^n \left( \frac{A_{2n}}{n} \cos \pi n + \frac{A_{2n}}{n} \right) \right\} .$$

If the two wave shapes are similar such that $A_{1n} = A_{2n}$, then

$$\left( \sigma_{x1}\Big|_{max} \right) \frac{\lambda_1}{2\pi} = \left( \sigma_{x2}\Big|_{max} \right) \frac{\lambda_2}{2\pi}$$

and using Eq. (4)

$$\sigma_{x1}\Big|_{max} f_1 = \sigma_{x2}\Big|_{max} f_2 . \tag{6}$$

The maximum value of $\sigma_{x1}$ is $\sigma_{x1}\Big|_{max}$ (cf. Eq. (2) ) and the extreme value of $\sigma_{x2}$ is $\sigma_{x2}\Big|_{max}$ i.e., $\sigma_{x2} = -\sigma_{x2}\Big|_{max}$ (cf. Eq. (3) ), then again

$$\sigma_{x1} f_1 = -\sigma_{x2} f_2 \tag{7}$$

for the conditions of identical wave form. This is identical to Eq. (1) when L and $\lambda$ are cancelled in the earlier equation. Hereafter the subscripts denoting maximum stress will be dropped, and $\sigma_{x1}$ and $\sigma_{x2}$ will be

used to indicate maximum values of these two stresses. Only stress maxima need be considered in the following analysis because dislocations will encounter the greatest barriers where the stresses are largest.

In the following, isotropic elasticity is first considered, but because of the significant anisotropy of metal crystals, equations will also be derived for use with the directionally dependent elastic properties.

For isotropic materials

$$\left.\begin{aligned} \epsilon_x &= \frac{1}{E}\ \{\sigma_x - \nu(\sigma_y + \sigma_z)\} \\ \epsilon_y &= \frac{1}{E}\ \{\sigma_y - \nu(\sigma_x + \sigma_z)\} \\ \epsilon_z &= \frac{1}{E}\ \{\sigma_z - \nu(\sigma_x + \sigma_y)\} \end{aligned}\right\} \tag{8}$$

where E is Young's modulus and $\nu$ is Poisson's ratio. Since $\sigma_x = \sigma_y$, and $\sigma_z = 0$

$$\epsilon_x = \frac{1}{E}\ \{\sigma_x - \nu\sigma_x\}$$

and

$$\sigma_x = \frac{E\ \epsilon_x}{1 - \nu}\ . \tag{9}$$

Substituting Eq. (9) into Eqs. (1) or (7)

$$\frac{E_1\ \epsilon_{x1}\ f_1}{1 - \nu_1} = -\ \frac{E_2\ \epsilon_{x2}\ f_2}{1 - \nu_2}\ . \tag{10}$$

Since $\epsilon_x = \dfrac{\bar{a} - a_o}{a_o}$ is the strain in the x direction of a plate ($a_o$ being the appropriate cubic lattice parameter) then

$$\frac{E_1 f_1 (\bar{a} - a_{10})}{(1 - \nu_1)\, a_{10}} = - \frac{E_2 f_2 (\bar{a} - a_{20})}{(1 - \nu_2)\, a_{20}} . \tag{11}$$

On solving Eq. (11) for $\bar{a}$

$$\bar{a} = \frac{a_{10} a_{20} \{(1 - \nu_2)\, E_1 f_1 + (1 - \nu_1)\, E_2 f_2\}}{a_{20} (1 - \nu_2) E_1 f_1 + a_{10} (1 - \nu_1) E_2 f_2} . \tag{12}$$

Equation (9) can be rewritten

$$\sigma_x = \frac{E\, (\bar{a} - a_o)}{(1 - \nu)\, a_o} \tag{13}$$

so that when the elastic constants and cubic lattice parameters of the two phases are known, the biaxial tension and compression stresses in phases 1 and 2, respectively, can be determined.

From Eqs. (8) and (9)

$$\epsilon_z = \frac{1}{E} \{\sigma_z - \nu(\sigma_x + \sigma_y)\}$$

$$= \frac{1}{E} \{0 - \nu\, (2\, \sigma_x)\}$$

$$= - \frac{2\nu\, \sigma_x}{E} = - \frac{2\nu\, E\, \epsilon_x}{(1 - \nu) E} = - \frac{2\nu\, \epsilon_x}{1 - \nu} .$$

Since $\epsilon_z = \dfrac{c - a_o}{a_o}$ and $\epsilon_x = \dfrac{\bar{a} - a_o}{a_o}$ then

$$\frac{c - a_o}{a_o} = - \frac{2\nu\, (\bar{a} - a_o)}{(1 - \nu)\, a_o}$$

and

$$c = \frac{1}{1 - \nu} \{ (\nu + 1)a_o - 2\nu \bar{a} \}. \tag{14}$$

Likewise, if the tetragonal data for c and $\bar{a}$ are known, the composition of the phase can be estimated from $a_o$ which is obtained by rearranging Eq. (14).

$$a_o = \frac{1}{1 + \nu} \{2\nu \bar{a} + (1 - \nu)c\}. \tag{15}$$

The equations for use with the anisotropic elastic compliances take much the same form as those for the isotropic case. Again the conditions of Eq. (1) or (7) apply. The equations for use with anisotropic cubic crystals which correspond to those of Eq. (8) for isotropic materials are

$$\left.\begin{aligned}
e_{xx} &= s_{11}\sigma_{xx} + S_{12}\sigma_{yy} + S_{12}\sigma_{zz} \\
e_{yy} &= S_{12}\sigma_{xx} + S_{11}\sigma_{yy} + S_{12}\sigma_{zz} \\
e_{zz} &= S_{12}\sigma_{xx} + S_{12}\sigma_{yy} + S_{11}\sigma_{zz} \\
e_{yz} &= S_{44}\sigma_{yz} \\
e_{zx} &= S_{44}\sigma_{zx} \\
e_{xy} &= S_{44}\sigma_{xy}
\end{aligned}\right\} . \tag{16}$$

The first subscript of the stresses and strains in Eq. (16) refers to the normal of the plane over which the stresses act while the second gives the direction of their action. Thus $e_{xx}$ and $\sigma_{xx}$ are equivalent to $e_x$ and $\sigma_x$ which appear in the equations for isotropic materials. $S_{11}$, $S_{12}$, and $S_{44}$ are the elastic compliances for cubic crystals. As before, $\sigma_{xx} = \sigma_{yy}$, and $\sigma_{zz} = 0$.

In addition, $\sigma_{xy} = 0$ because the two structures are tetragonal and the x-y plane is taken perpendicular to the four-fold axis of rotation. $\sigma_{yz}$ and $\sigma_{xz}$ are not zero, but for plates that are long compared to their thickness, these shear stresses are small. $\sigma_{yz}$ and $\sigma_{xz}$ will be greatest at the boundary between phases 1 and 2 where they are related to $\sigma_{xx}|_{max}$ by the ratio of $\lambda/L$. For thin plates $\lambda << L$ and $\lambda/L$ is small so that $\sigma_{yz}$ and $\sigma_{xz}$ can be neglected. Therefore

$$\left.\begin{aligned} e_{xx} &= (S_{11} + S_{12})\,\sigma_{xx} \\ e_{yy} &= (S_{11} + S_{12})\,\sigma_{xx} \\ e_{zz} &= 2S_{12}\,\sigma_{xx} \end{aligned}\right\} \tag{17}$$

and

$$\sigma_{xx} = \frac{e_{xx}}{S_{11} + S_{12}}. \tag{18}$$

Applying Eq. (1) or (7)

$$\frac{e_{xx_1} f_1}{(S_{11} + S_{12})_1} = - \frac{e_{xx_2} f_2}{(S_{11} + S_{12})_2} \tag{19}$$

where the subscripts outside the parentheses refer to the data for phase one and two respectively. By substituting $e_{xx} = \frac{\bar{a} - a_o}{a_o}$ into Eq. (19) $\bar{a}$ can be obtained as before (cf. Eq. (12) ).

$$\bar{a} = \frac{a_{10}a_{20}\,\{f_1(S_{11}+ S_{12})_2 + f_2(S_{11}+S_{12})_1\}}{a_{20}f_1(S_{11}+S_{12})_2 + a_{10}f_2(S_{11}+S_{12})_1} \tag{20}$$

If the elastic compliances and cubic lattice parameters are known, then Eq. (18) can be used to evaluate the principle stresses in each plate.

From Eqs. (17) and (18)

$$e_{zz} = \frac{2S_{12}e_{xx}}{S_{11} + S_{12}}$$

and $\frac{c - a_o}{a_o} = \frac{2S_{12}}{S_{11} + S_{12}} \frac{(\bar{a} - a_o)}{a_o}$, therefore

$$c = a_o + \frac{2S_{12}}{S_{11} + S_{12}} (\bar{a} - a_o) \tag{21}$$

or, as before, if $\bar{a}$ and the $c/\bar{a}$ ratio are known for each phase then the cubic parameters can be obtained by rearranging Eq. (21) and

$$a_o = \frac{1}{S_{11} - S_{12}} \{(S_{11} + S_{12})c - 2S_{12}\,\bar{a})\} . \tag{22}$$

In order to find the effects of $\sigma_{x1}$ and $\sigma_{x2}$ on dislocation motion, shear components of these stresses on the slip plane and in the slip direction must be found. For FCC crystals the slip plane is {111} and the slip direction is ⟨110⟩ . Resolution of these stresses can be done geometrically or with the aid of a stress tensor. On using the tensor method, the stress in the $\rho$ direction, when the normal to the slip plane is given by $\mu$, is

$$\sigma_{\mu\rho} = \sum_{ij} \sigma_{ij} \ell_{i\mu} \ell_{j\rho} \tag{23}$$

$$i = x, y, z$$

$$j = x, y, z$$

where $\ell_{i\mu}$ and $\ell_{j\rho}$ are direction cosines between the given lines. Letting $\mu$ be normal to the (111) plane and $\rho$ be in $[10\bar{1}]$, then, when the lamellar plates lie in the x-y plane,

$$\sigma_{(111)[10\bar{1}]} = \sigma_{xx}\,\ell_{[100][111]}\ell_{[100][10\bar{1}]} + \sigma_{xx}\ell_{[010][111]}\ell_{[010][10\bar{1}]}$$

where $\ell_{[100][111]} = \frac{1}{\sqrt{3}}$, $\ell_{[100][101]} = \frac{1}{\sqrt{2}}$ $\ell_{[010][111]} = \frac{1}{\sqrt{3}}$,

and $\ell_{[100[[10\bar{1}]} = 0$. Therefore $\sigma_{(111)[10\bar{1}]} = \sigma_{(111)[110]} = \frac{\sigma_{xx}}{\sqrt{6}}$.

Likewise, $\sigma_{(111)[01\bar{1}]} = \sigma_{(111)[\bar{1}10]} = \frac{\sigma_{xx}}{\sqrt{6}}$ but $\sigma_{(111)[\bar{1}10]} = 0$.

These stresses are pure shear components because $\rho$ is normal to $\mu$.

Figure 4 shows graphically the relationships of one potential slip plane and three potential slip directions to the stresses $\sigma_x$, $\sigma_y$, and $\sigma_z$. The lamella are considered to be parallel to the x-y plane in Fig. 4. The resolved shear stress from $\sigma_x$, $\sigma_y = \sigma_x$, and $\sigma_z = 0$ in the $[10\bar{1}]$ direction on the (111) plane is

$$\tau_{[10\bar{1}]} = \frac{\sigma_x}{\sin\theta}\,\frac{A_{(100)}}{A_{(111)}}\cos\phi\cos\psi$$

where $\theta = 45°$, $\cos\phi = \frac{1}{\sqrt{3}}$ and $\psi = 30°$. $\frac{A_{(100)}}{A_{(111)}} = \frac{1}{\sqrt{3}}$ is the ratio of the area of the (100) plane to the area of the (111) plane which projects onto the (100) plane. Therefore,

$$\tau_{[10\bar{1}]} = \sqrt{2}\sigma_x\,\frac{1}{\sqrt{3}}\,\frac{1}{\sqrt{3}}\,\frac{\sqrt{3}}{2} = \frac{\sigma_x}{\sqrt{6}}\,. \qquad (24)$$

Likewise,

$$\tau_{[01\bar{1}]} = \frac{\sigma_x}{\sqrt{6}}$$

and

$$\tau_{[\bar{1}10]} = 0\,.$$

These are the stresses encountered by the three possible dislocations (six if the negative signs are included) gliding on this (111) plane for lamellar plates lying parallel to (001), i.e., in the x-y plane of Fig. 4 .

Consider a dislocation in the (111) plane with Burger's vector $\frac{a}{2}[10\bar{1}]$. For plates which are parallel to (001) we have seen from Eqs. (23) and (24) that $\tau_{[10\bar{1}]} = \frac{\sigma_x}{\sqrt{6}}$ . An adjoining set of plates will be parallel to either (010) or (100). For plates parallel to (010) $\sigma_x = \sigma_z$ and $\sigma_y = 0$ so that the shear stress acting on the above dislocation while it is in these plates is

$$\tau_{[10\bar{1}]} = \sigma_{xx}\ell_{x\mu}\ell_{x\rho} + \sigma_{zz}\ell_{z\mu}\ell_{z\rho}$$

$$= \sigma_{xx}\frac{1}{\sqrt{3}}\frac{1}{\sqrt{2}} + \sigma_{xx}\frac{1}{\sqrt{3}}\left(-\frac{1}{\sqrt{2}}\right) = 0 .$$

For plates parallel to (100), $\sigma_x = 0$, and $\sigma_y = \sigma_z$ so that

$$\tau_{[10\bar{1}]} = \sigma_{yy}\ell_{y\mu}\ell_{y\rho} + \sigma_{zz}\ell_{z\mu}\ell_{z\rho}$$

$$= \sigma_{yy}\frac{1}{\sqrt{3}}(0) + \sigma_{yy}\frac{1}{\sqrt{3}}\left(-\frac{1}{\sqrt{2}}\right) = -\frac{\sigma_{yy}}{\sqrt{6}} .$$

Since a dislocation will interact with these three plate orientations with equal probability, one-third of a unit length of dislocation will experience an accelerating stress from plates parallel to (001) when $\sigma_x > 0$, one-third will experience zero stress from plates parallel to (010), and the remainder will experience a retarding stress from plates parallel to (100) when $\sigma_y > 0$. The portion of the dislocation which is accelerated will move until it encounters an adjacent tetragonal plate that is loaded in compression so that $\sigma_x < 0$ and $\tau_{[10\bar{1}]} = -\frac{|\sigma_x|}{\sqrt{6}}$, which is now a retarding stress. Consequently, the dislocation will be retarded along one-third of its length by plates which are in compression, experience zero stress

along one-third of its length, and be retarded along the remaining third by plates that are loaded in tension. Dislocations in other slip systems will encounter identical conditions. The maximum retarding force on a unit dislocation will be, then

$$F = \frac{1}{3}\,|\tau_1|b + \frac{1}{3}|\tau_2|b + 0 \tag{25}$$

where $|\tau_1|$ is the absolute value of the resolved shear stress acting on dislocations with Burgers vector b from plates which are in tension (for plate orientations where $\tau_1 \neq 0$) and $|\tau_2|$ is the absolute value of the resolved shear stress from plates which are in compression (for plate orientations where $\tau_2 \neq 0$). Now $|\tau_1| = \frac{\sigma_{x_1}}{\sqrt{6}}$ and $|\tau_2| = -\frac{\sigma_{x_2}}{\sqrt{6}}$ so that $F = \frac{1}{3}\,\frac{1}{\sqrt{6}}\,(\sigma_{x_1} - \sigma_{x_2})b$ where the negative sign appears before $\sigma_{x_2}$ because of its compressive nature. The applied stress which must overcome this force if dislocations are to move is $\tau_{app} = \frac{F}{b}$ or

$$\tau_{app} = \frac{1}{3\sqrt{6}}\,(\sigma_{x_1} - \sigma_{x_2}) \quad . \tag{26}$$

However, when $\tau_{app} > |\tau_2|$, which can happen when $f_2$ is large and phase 2 contains a small strain, then Eq. (26) no longer governs the stress for the first dislocation motion. In this case the applied stress will cause the dislocation segment inhibited by $\tau_2$ to move through phase 2 until it reaches phase 1 where it will be accelerated. Then only one-third of the unit length of dislocation line will be retarded while the other two segments will have either zero shear stress or an accelerating stress. The net effect is that plastic flow can easily take place. The applied stress $\tau_{app}$ needed to start this chain of events is

$$\tau_{app} = |\tau_2| = -\frac{\sigma_{x2}}{\sqrt{6}} \quad . \tag{27}$$

$\tau_1$ and $\tau_2$ are dependent on the volume fractions of the two phases present. By equating the applied stress to $|\tau_2|$ in Eq. (26), a solution for the critical volume fraction where Eq. (26) will break down can be obtained. Assume that the elastic moduli are the same in both phases. Therefore,

$$|\tau_2| = -\frac{\sigma_{x_2}}{\sqrt{6}} = \frac{1}{3\sqrt{6}}\left(\sigma_{x_1} - \sigma_{x_2}\right)$$

and

$$2\sigma_{x_2} = -\sigma_{x_1}$$

or

$$\frac{2(\bar{a} - a_{20})}{(S_{11} + S_{12})a_{20}} = -\frac{(\bar{a} - a_{10})}{(S_{11} + S_{12})a_{10}}$$

and on solving for $\bar{a}$

$$\bar{a} = \frac{a_{10}a_{20}}{\frac{1}{3}a_{20} + \frac{2}{3}a_{10}} . \tag{28}$$

The critical volume fraction $f_2$ can be found by comparing Eq. (28) to either Eqs. (12) or (20) because when the elastic constants are the same in both phases both Eqs. (12) and (20) reduce to

$$\bar{a} = \frac{a_{10}a_{20}\ \{f_1 + f_2\}}{f_1 a_{20} + f_2 a_{10}} .$$

Thus, $f_2 = \frac{2}{3}$ and $f_1 = \frac{1}{3}$. Similar equations can be derived when $\tau_{app} = |\tau_1|$. The solution for this case will give $f_1 = \frac{2}{3}$ and $f_2 = \frac{1}{3}$ when the elastic moduli are equal. Under equal moduli conditions Eq. (26) is good for $\frac{1}{3} \leq f_1 \leq \frac{2}{3}$. When the moduli are not the same in both phases, an independent check of Eq. (26) can be made for each set of data to see if the conditions $\tau_{app} \leq |\tau_1|, |\tau_2|$ are met.

The four important equations derived above for the isotropic case are:

$$\text{I.} \qquad \bar{a} = \frac{a_{10}a_{20}\{(1-\nu_2)E_1f_1 + (1-\nu_1)E_2f_2\}}{a_{20}(1-\nu_2)E_1f_1 + a_{10}(1-\nu_1)E_2f_2} \tag{12}$$

$$\text{II.} \qquad \sigma_x = \frac{E(a - a_o)}{(1-\nu)a_o} \tag{13}$$

$$\text{III.} \qquad \tau_{app} = \frac{1}{3\sqrt{6}}(\sigma_{x_1} - \sigma_{x_2}) \tag{26}$$

when $\tau_{app} \leq |\tau_1|, |\tau_2|$

$$\text{IV.} \qquad \tau_{app} = |\tau_2| = -\frac{\sigma_{x_2}}{\sqrt{6}} \tag{27}$$

if $|\tau_2| < |\tau_1|$ and the conditions of Eq. (26) are not met.

If $|\tau_1| < |\tau_2|$ and Eq. (26) does not apply, then $\tau_{app} = |\tau_1|$.

The corresponding equations for the anisotropic case are:

$$\text{I.} \qquad \bar{a} = \frac{a_{10}a_{20}\{(S_{11} + S_{12})_2\ f_1 + (S_{11} + S_{12})_1\ f_2\}}{a_{20}(S_{11} + S_{12})_2\ f_1 + a_{10}(S_{11} + S_{12})_1\ f_2} \tag{20}$$

$$\text{II.} \qquad \sigma_{xx} = \frac{(a - a_o)}{(S_{11}+S_{12})a_o} \tag{18}$$

$$\text{III.} \qquad \tau_{app} = \frac{1}{3\sqrt{6}}(\sigma_{xx1} - \sigma_{xx2}) \tag{26}$$

when $\tau_{app} \leq |\tau_1|, |\tau_2|$

$$\text{IV.} \qquad \tau_{app} = |\tau_2| = -\frac{\sigma_{xx_2}}{\sqrt{6}} \tag{27}$$

if $|\tau_2| < |\tau_1|$ and the conditions of Eq. (26) are not met. If $|\tau_1| < |\tau_2|$ and Eq. (26) does not apply, then $\tau_{app} = |\tau_1|$.

Thus, when the elastic constants, volume fractions, and cubic lattice parameters for the extreme conditions are known, the critical resolved

shear stress can be calculated for a wide range of conditions. For $f_1 \ll \frac{1}{3}$, Eq. (27) will not be valid because of the loss of uniform strain fields for small volume fractions of precipitate.

If $\nu_1 = \nu_2$ and $E_1 = E_2$, then for the isotropic case

$$\bar{a} = \frac{a_{10}a_{20}(f_1 + f_2)}{a_{20}f_1 + a_{10}f_2}$$

$$\sigma_{x_1} = \frac{E(\bar{a} - a_{10})}{(1-\nu)a_{10}} = \frac{E}{1-\nu}\left\{\frac{a_{20}}{a_{20}f_1 + a_{10}f_2} - 1\right\}$$

$$\sigma_{x_2} = \frac{E}{1-\nu}\left\{\frac{a_{10}}{a_{20}f_1 + a_{10}f_2} - 1\right\}$$

and

$$\tau_{app} = \frac{1}{3\sqrt{6}}\left\{\frac{a_{20} - a_{10}}{a_{20}f_1 + a_{10}f_2}\right\} \tag{29}$$

but because $a_{10} \approx \bar{a} \approx a_{20}$

$$\tau_{app} \approx \frac{1}{3\sqrt{6}}\frac{E}{1-\nu}\left(\frac{\Delta a_o}{\bar{a}}\right) \tag{30}$$

For the anisotropic case, if $(S_{11} + S_{12})_1 = (S_{11} + S_{12})_2$, then a similar derivation leads to

$$\tau_{app} = \frac{1}{3\sqrt{6}}\frac{1}{(S_{11} + S_{12})}\left\{\frac{a_{20} - a_{10}}{a_{20}f_1 + a_{10}f_2}\right\} \tag{31}$$

or

$$\tau_{app} \approx \frac{1}{3\sqrt{6}}\frac{1}{(S_{11} + S_{12})}\left(\frac{\Delta a_o}{\bar{a}}\right) \tag{32}$$

Thus the yield stress is directly proportional to the difference in lattice parameters of the two extreme compositions when Eq. (26) is valid. Usually the elastic moduli do not differ widely so that this is an approximately general result.

When $\tau_{app}$ is given by Eq. (27), a general relationship between yield stress and volume fraction can be obtained if it is again assumed that the elastic moduli are the same in both phases. From Eqs. (27), (24), and (18)

$$\tau_{app} = |\tau_2| = -\frac{\sigma_{xx_2}}{\sqrt{6}} = -\frac{1}{\sqrt{6}} \frac{(\bar{a} - a_{20})}{(S_{11}+S_{12})a_{20}}$$

but when the elastic moduli are the same, Eq. (20) gives

$$\bar{a} = \frac{a_{10}a_{20}}{a_{20}f_1+a_{10}f_2} \qquad \text{and}$$

$$\tau_{app} = -\frac{1}{\sqrt{6}} \frac{1}{(S_{11}+S_{12})} \{\frac{a_{10}}{a_{20}f_1+a_{10}f_2} - 1\}, \text{ and rearranging}$$

$$\tau_{app} = -\frac{1}{\sqrt{6}} \frac{1}{(S_{11}+S_{12})} \{\frac{a_{10}f_1-a_{20}f_1}{a_{20}f_1-a_{10}f_1+a_{10}}\}, \text{ or}$$

$$\tau_{app} = -\frac{1}{\sqrt{6}} \frac{1}{(S_{11}+S_{12})} \{\frac{-\Delta a_o}{\Delta a_o+a_{10}/f_1}\}, \text{ and}$$

$$\tau_{app} = \frac{1}{\sqrt{6}} \frac{1}{(S_{11}+S_{12})} \frac{1}{1 + \frac{a_{10}}{\Delta a_o f_1}}$$

but $\frac{a_{10}}{\Delta a_o f_1} \gg 1$

and

$$\tau_{app} = \frac{1}{\sqrt{6}} \frac{f_1}{(S_{11}+S_{12})} \left(\frac{\Delta a_o}{a_{10}}\right) \tag{33}$$

for $f_1 < f_1^{min}$ where $f_1^{min} \approx \frac{1}{3}$ and is established by Eq. (26) when $\tau_{app} = |\tau_2|$. Thus the yield stress is directly proportional to the difference in cubic lattice parameters and the volume fraction of phase one for these conditions.

The critical resolved shear stress can be obtained experimentally from oriented single crystal tensile specimens with the aid of the Schmid factor. However, polycrystalline samples are adequate to check a number of the points of the theory. Absolute values of the tensile yield stress can be calculated on the basis of theories[16] for the plastic deformation of polycrystalline samples which gives

$$\bar{\sigma}_{yield} = \bar{m}\,\tau_{yield} \tag{34}$$

where the constant $\bar{m}$ involves an average orientation factor for the slip systems which operate during plastic flow. The equation used for calculating tensile yield stresses of polycrystalline samples thus becomes

$$\sigma_{yield} = \frac{\bar{m}}{3\sqrt{6}}\left(\sigma_{xx_1} - \sigma_{xx_2}\right) \tag{35}$$

For randomly oriented grains $\bar{m} = 3.06$.

The samples used in checking the theory were forged or swaged which gives rise to a texture with some grains having [100] near the tensile axis and others with [111] parallel to the bar axis.[17] This texture is retained after annealing.[18] The Schmid factor for [100] crystals would be equivalent to using $m = 2.45$ while that for [111] grains would correspond to $\bar{m} = 3.68$. Since [100] is the more favorable orientation of the two for slip, grains in this orientation will contribute more to the initial yielding process. Therefore an $\bar{m}$ constant between 2.45 and 3.06 would be appropriate for calculating the absolute values of the yield stresses for fabricated polycrystalline bars.

The equations derived above show four significant points:

1) The yield stress is independent of $\lambda$, the modulated structure wavelength, which means the yield stress is independent of particle size.

2) The yield stress is nearly independent of the volume fractions $f_1$ and $f_2$ if the elastic constants do not differ appreciably in the two phases and Eq. (26) applies.

3) The yield stress is directly proportional to the difference in cubic lattice constants of the precipitating phases when the elastic constants are nearly the same in both phases and Eq. (26) applies.

4) When $f_1 < f_1^{min}$, or $f_1 > f_1^{max}$ where $f_1^{min} \approx \frac{1}{3}$ and $f_1^{max} \approx \frac{2}{3}$ are the critical volume fractions where Eq. (26) becomes invalid, the yield stress is directly proportional to the difference in cubic lattice parameters and the volume fraction of the precipitating phase providing the elastic moduli are the same in both precipitate and matrix.

## III. EXPERIMENTAL PROCEDURE

Four compositions of polycrystalline Cu-Ni-Fe samples were prepared and these are designated as alloys 1, 2, 3, and 4 in Fig. 1 and Table I. Compositions were verified by chemical analysis. Alloys 1, 2, and 3 lie on one tie line. The alloys were cast into one-half inch diameter copper molds in an inert atmosphere, forged (alloys 1-3) or swaged (alloy 4) to three-eighth inch diameter rod, and homogenized for three days at 950°C in evacuated quartz capsules. Before melting, 0.5 wt.% manganese was added to each alloy to aid fabrication. The average grain size of the homogenized bars was 0.15 mm. Tensile bars with a gauge length of 1.125 inches and diameter of 0.160 inches were ground from the homogenized bars, encapsulated in evacuated quartz tubes, heated to 950°C, and quenched in water before aging. Alloys 1-3 were aged at 625°C for various times or aged first at 625°C for a specified time and then given a subsequent treatment at 450°C for 100 hours. Daniel[6] has shown that the length of time at the higher temperature fixes the wavelength of the composition fluctuation while the lower temperature influences the amplitude of the fluctuation. Samples of alloy 4 were aged to their maximum hardness at 800°C, 730°C, and 625°C to independently check the effect of variation in lattice constants of the two precipitating phases. An additional sample of alloy 4 was first aged 6 hours at 625°C and then held 100 hours at 550°C. It was necessary to quench the samples after aging at temperatures above 625°C to prevent structural changes from occurring while cooling to room temperature. An Instron tensile testing machine was employed using a strain rate of .0175 in/in/min and the yield stresses were determined by the .02% offset method.

Lattice parameters of the two equilibrium phases were determined from alloy 4 for the three aging temperatures 800°C, 730°C, and 625°C. Powder samples were held 15 days at 800°C and one month at 730°C and 625°C. A back reflection focusing camera of 60 mm radius and unfiltered chromium radiation were used for the lattice parameter determinations.

## IV. EXPERIMENTAL RESULTS

Figure 5 shows the measured yield stress versus aging time data for alloy 2. The yield stress reaches its maximum rapidly and maintains a value very near the maximum even after 194 hours at 625°C. The other alloys (1-3) revealed similar trends at 625°C as did the alloys given the additional 450°C treatment, but the yield stresses of tensile specimens given the additional treatment were shifted to higher values. Table II gives the maximum measured values taken from the yield point vs. aging time curves for alloys 1,2, and 3 aged at the two temperatures. The aging time to maximum yield was either 8 hours at 625°C or 8 hours at 625°C plus 100 hours at 450°C. Table III gives the experimental yield stresses for samples of alloy 4 after aging them to their maximum hardness which occurred after holding for 3 minutes at 800°C, 16 minutes at 730°C, and 8 hours at 625°C. The yield stress of the alloy 4 sample which was held at 625°C for 6 hours and then 100 hours at 550°C is also given in Table III.

## V. DISCUSSION OF RESULTS

Experimental verification of the theory is limited to the conditions under which Eq. (26) is valid. First, confirmation will be made of three of the four significant points indicated by the equations which were derived in Sec. II:

1) The wavelength of the modulated structure is directly related to the aging time.[5,8,10] Values of the modulation wavelength measured by Hillert et al.[10] on their alloy H, an alloy with a composition near to that of alloy 2, are placed in parentheses at the appropriate times in Fig. 5. These wavelengths are given in numbers of atomic planes. It is clear from Fig. 5 that the yield stress does not vary greatly with aging time or modulation wavelength. This agrees with the theory in that $\lambda$ does not appear in Eqs. (12), (13), (26), and (34) or in the similar Eqs. (18), (20), (26), and (34).

2) The volume fractions of the two precipitating phases are different for each of the alloys 1-3 although the phase compositions are the same for any given temperature since these alloys all lie on the same tie line. Table II shows that the maximum yield stress is constant for these three alloys when they have been aged at the same temperature. Therefore the yield stress does not change as a function of the volume fraction. Changes in the calculated yield stresses with changes in volume fraction mainly reflect the difference in elastic moduli of the two phases. Since the experimental yield stresses do not change with changes in volume fraction, then the converse is indicated, i.e., there is no difference in the elastic moduli of the two phases. Thus, Eq. (32), which shows no dependence upon volume fraction, can be applied.

The conditions under which Eq. (26) is valid were checked for alloys 1 and 3 because they have volume fractions very near the critical values determined in Sec. II. It was found that Eq. (26) could be applied to both alloys within the uncertainty of establishing the critical and estimated volume fractions for alloys which lie on this tie line. The experimental results in Table II show Eq. (26) to be valid.

3) Equation (32) (in conjunction with Eq. (34)) suggests that a plot of measured yield stress versus $\Delta a_o$ would produce a straight line passing through the origin, i.e., the yield stress is directly proportional to $\Delta a_o$. Equation (32) requires equal elastic moduli in the two phases but the proportionality between yield point and $\Delta a_o$ is quite constant for any one alloy even if the moduli are different. This is difficult to establish analytically; however, a graphical example shows it to be true. The points in Fig. 6 designated by squares represent calculated yield stresses ($\bar{m} = 2.5$) which were computed for alloy 4 using different elastic compliances for each phase. These points lie on the solid line which extrapolates to the origin as required by direct proportionality. Figure 6 shows plots of the measured peak yield stress versus the difference in lattice parameters of the equilibrium cubic phases for alloys 1-3 (circles) and versus the difference in cubic lattice parameters calculated from tetragonal lattice parameter data for alloy 4 (triangles). (The method of evaluating $\Delta a_o$ from tetragonal data will be discussed later.) The points on both lines are easily within the accuracy of the yield point data or especially, in the case of alloy 4, within the accuracy of the method of determining $\Delta a_o$ from tetragonal data. The data thus give a confirmation of the direct proportionality between yield stress and $\Delta a_o$.

The slopes of the lines in Fig. 6 depend on the proportionality factor of Eq. (32) or, in a more complicated way, on Eqs. (18), (20), (26), and (34). In order to make calculations using these equations, the required data for Cu-Ni-Fe alloys must be assembled. The sources of these data will be discussed next:

1) Volume fractions were obtained in all cases from the phase diagram with the aid of the lever law. These values are incorporated in Table I with the alloy compositions.

2) The elastic compliances for the component phases were estimated by first assuming that the elastic anisotropy of the copper-rich phase is the same as for pure copper and that of the copper-poor phase is the same as for pure nickel. Values of Young's modulus were obtained for pure copper and for copper-nickel alloys of about the same composition as that of the precipitating copper-rich phase. The elastic compliances for the copper-rich phase were then estimated by scaling down the pure copper elastic compliance data in the ratio of the Young's modulus of pure copper to the modulus of the copper-nickel alloy. A similar method was used for the copper-poor phase but this time nickel data were scaled up in the ratio of the Young's modulus for pure nickel to that of the proper nickel-iron alloy. This is justified by the equation used for calculating Young's modulus from single crystal elastic data if the anisotropy of the alloy and the pure element are the same, i.e.,

$$\frac{1}{\overline{E}} = S_{11} + \frac{2}{5}\left(S_{12} + \frac{S_{44}}{2} - S_{11}\right)$$

Here $\overline{E}$ is Young's modulus (for polycrystals), $S_{11}$, $S_{12}$, and $S_{44}$ are elastic compliances of individual grains, and the $\frac{2}{5}$ factor arises from

an average grain orientation consideration. The equation shows that a proportional change in each of the elastic compliances will result in an inverse change in $\bar{E}$. The required data for making estimates of the elastic compliances are included in Table IV. The values from lines 3 and 4 of Table IV were used for alloys 1-3 and those from lines 5 and 6 were used for alloy 4 calculations. The sum $S_{11} + S_{12}$ is also included because it regularly appears in the equations.

3) Lattice constants (in kx units) for the cubic phases in equilibrium in alloys 1-3 were obtained from the lattice parameter contours published by Bradley et al.[2] The compositions of the phases in equilibrium at the given temperatures were obtained from the Cu-Ni-Fe phase diagram.[1] The constants obtained from the literature for alloys 1-3 along with the measured parameters for alloy 4 aged at the different temperatures are given in Table V.

The lattice parameters measured on a sample of alloy 4 which had been annealed at 800°C agreed with the values obtained by Hargreaves[7] on the same alloy ($Cu_{10}Ni_7Fe_3$) and for the same annealing temperature. These parameters are good to approximately four significant figures. Values of $\bar{a}$ calculated from Eq. (20) are also given in Table V.

In addition, Hargreaves[7] gave tetragonal lattice parameters for $Cu_{10}Ni_7Fe_3$ aged to the tetragonal stage at three temperatures. These parameters are given in Table VI along with values of $a_{10}$ and $a_{20}$ calculated from Eq. (22). A comparison of the calculated values of $\bar{a}$ in Table V with the measured values in Table VI shows a fine agreement. This is consistent with the initial assumption that coherency strains are causing the tetragonal distortions.

The difference in measured and calculated cubic parameters also shows an effect which has been mentioned previously. Since the values are given for different temperatures in Tables V and VI the comparison can best be made on a graph. Figure 7 shows that the cubic parameters calculated from tetragonal data (dashed line) lie inside the measured cubic data (solid line) except at the highest temperature. This indicates that strain energy which increases at lower temperatures during the tetragonal stage of the transformation inhibits the approach of the two phases to their equilibrium compositions. Strain energy increases with the square of the strain and therefore becomes significant at larger strains.

The method of calculating $a_o$'s from tetragonal data (Eq. 22) appears to be right because of the close agreement of the calculated values with the measured values at the smaller strain, i.e., for the alloy aged at 800°C. The values of $a_o$ used to determine $\Delta a_o$ at 625°C and 730°C for the graph in Fig. 6 were taken at the appropriate temperatures from the dashed lines in Fig. 7.

Calculated yield stresses which appear in Table II for alloys 1-3 were obtained using the equations for anisotropic materials, e.g., Eqs. (18), (20), (26), and (34). In this case $\bar{a}$ was obtained from the cubic lattice parameters. The calculated yield stresses for alloy 4, Table III, were obtained using the measured tetragonal $\bar{a}$ parameters while $a_o$'s were computed from Eq. (22). Direct substitution of $a_{10}$, $a_{20}$, and $\bar{a}$ in Eq. (20) and use of Eqs. (26) and (34) gave the desired results for alloy 4. Two values of $\bar{m}$ (Eq. 34) were used. The calculated yield stresses given in the column of Tables II and III with $\bar{m} = 3.06$ are for polycrystalline bars with randomly oriented grains. The values in Table II with $\bar{m} = 2.75$ and Table III with $\bar{m} = 2.5$ take into consideration the preferred

orientation which occurred during fabrication. These two particular values of $\bar{m}$ were selected because they gave the best fit to the data. Preferred orientation was observed to be important. Tensile samples of alloy 4 made from severely cold rolled and annealed stock with the tensile axis the same as the rolling direction had significantly lower yield stresses for the same heat treatment than the swaged and annealed bars. For example, rolled samples aged at 730°C and 625°C had yield stresses of 36,000 and 43,300 psi while the corresponding swaged bars had yields of 40,900 and 53,600 psi, respectively. Rolled stock of this material has been shown to have a [112] preferred orientation along the rolling direction[18,19] which is very near to the orientation which gives a minimum value to $\bar{m}$, i.e., $\bar{m} \geq 2$. Samples of alloys 1-3 were fabricated by forging while alloy 4 samples were swaged. This difference in fabrication procedure could result in the slight difference in $\bar{m}$ observed in Tables II and III for the best data fit. Also, the elastic moduli of the phases which precipitate for alloys 1-3 and alloy 4 are different and it is extremely hard to account exactly for this difference without making experimental measurements on crystals of these phases. Since the slope of the yield stress versus difference in cubic lattice parameter plot is dependent on both $\bar{m}$ and the elastic constants, the use of an $\bar{m}$ to give the best data fit is intended to normalize the unknown differences in both texture and moduli. The agreement without these corrections is good considering the uncertainty in estimating the elastic moduli for the precipitating phases. No attempt was made to correct for changes in moduli of phases which change composition at different aging temperatures.

The rolled samples discussed above were not quenched after aging while the swaged bars were and therefore the 730°C rolled sample value of 36,000

psi is slightly larger than it would have been had the sample been quenched after aging. The effect of hardening during cooling from the aging temperature was markedly observed on samples aged at 800°C. Samples of alloy 4 aged and relatively slowly cooled had a maximum hardness of $R_B82$ while those quenched after the aging treatment had a maximum hardness of $R_B69$. Also, since the transformation is hard to control at high temperatures it is probable that the peak of the yield versus aging time curve was not attained exactly for the 800°C sample of alloy 4 and this would explain why the 800°C yield stress appears to be low (cf. Fig. 6 and Table III). Having considered both experimental and calculated results, it is now possible to introduce new details involved in the yield stress of Cu-Ni-Fe and other alloys.

Earlier in the discussion it was shown that the volume fractions $f_1$ and $f_2$ do not greatly influence the yield stress for any one aging temperature if they are between certain critical limits. If the compliances of the two precipitated phases are the same, Eq. (18) shows that $f_1$ and $f_2$ are only weighting factors which balance $\bar{a}$ proportionately toward one cubic parameter or the other. That is, if $f_2$ is large (phase one is much thinner than phase two), then $\bar{a}$ will be close to $a_{20}$. This means that there will be very little elastic strain in phase two and a large amount of strain in phase one. Thus, if one of the phases is much thinner than the other, the strain in it is much larger and, consequently, the stress in it contributes most to the increase in yield stress (cf. Eq. (26)). Equation (32) shows that when the elastic compliances are the same in both phases, the yield stress does not depend greatly on which phase is highly stressed but depends only on the sum of the strains in the two phases. Since the total strain is dependent on $\Delta a_o$, the difference in cubic parameters of the extreme

compositions, and $\Delta a_o$ is independent of $f_1$ and $f_2$, the yield stress is relatively independent of $f_1$ and $f_2$.

When $f_1$ becomes smaller than the critical value, as discussed in Sec. II, then the maximum yield stress will fall off linearly with volume fraction (cf. Eq. (33)) until the strain fields are no longer uniform. Then the change with volume fraction will be more complicated. This is the case for most precipitation hardening systems. It is clear from this discussion that the equations derived in Sec. II give the maximum attainable yield stress for any precipitation hardening system where coherency strains are controlling because the yield stress does not increase after the critical volume fraction is exceeded.

It was shown through Fig. 7 that the extreme compositions of the phases existing during the transformation are not always given by the equilibrium compositions of the phase diagram. The actual difference in lattice parameter is usually somewhat less than that given for equilibrium phases because the driving force of the reaction is not sufficient to provide the strain energy needed for coherent equilibrium-composition plates. Many miscibility gap systems, e.g., Au-Pt and Cu-Ni-Co, have larger equilibrium parameter differences than Cu-Ni-Fe and thus the strain energy can become very large during the phase transformation. The yield stress determined for Au-40 at.% Pt was 110,000 psi for alloys aged at 500°C.[15] The equilibrium $\Delta a_o$ is .115Å which gives a computed yield* of 266,000 psi.

---

* It was observed for Cu-Ni-Fe alloys that a value of $\bar{m} = 2$ could be used to obtain the correct answer for the absolute yield stress when the equations for isotropic materials were used. In the following, this procedure is used in yield stress estimates for systems other than Cu-Ni-Fe.

R. Carpenter[15] estimated that the actual $\Delta a_o$ was about .029 in the grain interiors of Au-Pt during the transformation which results in a more reasonable yield stress of 69,000 psi. A value of $\Delta a_o$ = .046 would give the observed yield. Another example is provided by the hardness increase in Cu-Ni-Co.[20] Contrary to Cu-Ni-Fe where the hardness rapidly reaches a maximum with isothermal aging time and stays there, Cu-Ni-Co alloys show a more usual age-hardening response by slowly increasing to a maximum hardness and then overaging.[20] The difference in lattice parameters ($\Delta a_o$ = .058 at 600°C)[20] of the two phases in equilibrium in Cu-Ni-Co is about twice that for Cu-Ni-Fe and the strain energy is correspondingly much larger. Since the big factor in the yield stress of these alloys is $\Delta a_o$, this must be the parameter that is changing during the slow rise to maximum hardness which results in isothermal aging of Cu-Ni-Co alloys. A calculated value of the yield stress maximum for Cu-Ni-Co was 140,000 psi using equilibrium $a_o$'s while a rough experimental value estimated from hardness data was 120,000 psi.

Because the driving force is greater for alloys near the center of the miscibility gap, the maximum yield stress will probably be greater there due to the higher strains permissible. Only in alloys like Cu-Ni-Fe where the strains are relatively small will the yield stress be independent of the volume fractions of the precipitating phases between the critical values.

It was at first thought that ordering of the copper-poor phase ($Ni_3Fe$) was partially responsible for the increase in yield of alloys 1-3 after the 450°C treatments. Wakelin and Yates[21] have shown that $Ni_3Fe$ with up to four atomic percent copper will order on slowly cooling from 510°C to 400°C. It is difficult to prove the presence of order in $Ni_3Fe$ by

x-ray or other techniques so it was not certain that the copper-poor phase did order at 450°C. However, the trend in the yield stress increase indicated by an order-strengthening theory[22] was not observed. That is, the increase in yield of the 450°C aged alloys over those aged at 625°C did not show a large dependence on volume fraction of the ordered phase but instead exhibited a constant increase for all volume fractions (cf. Table II). This constant increase is consistent with the predictions of the present theory as is the calculated magnitude of the strength increase. To eliminate the complications of the ordering phenomena, alloy 4 was aged at temperatures above the ordering temperature. The yield stress data for alloy 4 fit the theory nicely and therefore it is certain that the yield increase of alloys 1-3 aged at 450°C over those aged at 625°C is due to increased coherency strains and is not due to ordering. The strong possibility that ordering is occurring in the copper-poor phase at 450°C suggests that ordering of lamellar precipitates does not cause large strength increases. It is well-known that materials which will order do not show significant differences in yield stress between the unordered and the fully ordered state.

## VI. CONCLUSIONS

1. Theory and experiment show that the yield stress of aged Cu-Ni-Fe alloys is nearly independent of the modulation wavelength of the composition fluctuations.

2. Theory and experiment show that the yield stress of aged Cu-Ni-Fe alloys is not appreciably changed by variations in the volume fractions of the two components when the volume fractions are between certain limits.

3. Theory and experiment show a direct proportionality between yield stress and the difference in the cubic lattice parameters of the two extreme compositions which are present in aged Cu-Ni-Fe alloys.

4. It has been shown that the strained coherent precipitates do not reach the compositions determined by the phase diagram for low aging temperatures when strain energy in the precipitates becomes significant.

## ACKNOWLEDGEMENTS

The author wishes to express his appreciation to Professor Earl R. Parker for his supervision of this work and to Professor R. Hultgren and Professor A. Pabst for their review of the thesis manuscript.

This research was supported by the United States Atomic Energy Commission.

## REFERENCES


1. Köster, W., and W. Dannöhl, Z. Metall., 27, 220 (1935).
2. Bradley, A. J., W. F. Cox, and H. J. Goldschmidt, J. Inst. Metals, 67, 189 (1941).
3. Bradley, A. J., Proc. Phys. Soc., 52, 80 (1940).
4. Daniel, V. and H. Lipson, Proc. Roy. Soc., A181, 368 (1943).
5. Daniel, V. and H. Lipson, Proc. Roy. Soc., A181, 378 (1944).
6. Daniel, V., Proc. Roy. Soc., 192, 575 (1947).
7. Hargreaves, M. E., Acta Cryst., 4, 301 (1951).
8. Biedermann, E. and E. Kneller, Z. Metall., 47, 289 (1956).
9. Biedermann, E. and E. Kneller, Z. Metall., 47, 760 (1956).
10. Hillert, M., M. Cohen, and B. L. Averbach, Acta Met., 9, 536 (1961).
11. Tiedema, T. J., J. Bowman, and W. G. Burgers, Acta Met., 5, 310 (1957).
12. Bagaryatskii, Yu A. and Yu D. Tyapkin, Kristallografiya 5, 535 (1960).
13. Bagaryatskii, Yu A. and Yu D. Tyapkin, Kristallografiya 5, 882 (1960).
14. Kelly, A. and R. B. Nicholson, Progress in Materials Science, 10, (Pergamon Press, New York, 1963) p. 149.
15. Carpenter, R., Strengthening Effects of Spinodal Decomposition in Gold-Platinum Alloys and the Kinetics of the Reaction, Ph.D. Thesis, University of California, 1966.
16. Cottrell, A. H., Dislocations and Plastic Flow in Crystals, (Clarendon Press, Oxford, England, 1953) p. 116.
17. Barrett, C. S., Structure of Metals, (McGraw-Hill Book Co., Inc., New York, 1952) p. 443.
18. Ibid., p. 499.
19. Ibid., p. 458.

20. Geisler, A. H. and J. B. Newkirk, Trans. AIME, 180, 101 (1949).

21. Wakelin, R. J. and E. L. Yates, Proc. Phys. Soc., London B66, 221 (1953).

22. Williams, R. D., Acta Met., 5, 241 (1957).

## FIGURE CAPTIONS

Fig. 1 Isothermal section for 600°C of the Cu-Ni-Fe phase diagram showing the compositions of alloys 1-4 investigated in this study. The portion of the diagram near the iron corner is omitted because it is irrelevant to the present investigation.

Fig. 2 Dark field electron micrograph of alloy 4 aged 20 minutes at 800°C.

Fig. 3 Model used to determine the stresses in coherent lamellar plates. Front surface (shaded) represents a plane cut through the lamella and the forces $F_{x1}$ and $F_{x2}$ represent replacements for the constraints which were removed by cutting.

Fig. 4 Diagram for determining the shear stresses effective on the slip plane due to coherency stresses in plates lying in the x-y plane.

Fig. 5 Measured yield stress vs. aging time at 625°C for alloy 2. Numbers in parentheses are approximate modulation wavelengths given in numbers of atomic planes.[10]

Fig. 6 Measured yield stresses for alloys 1-3 (circles) and alloy 4 (triangles) vs. difference in cubic lattice parameters of the precipitating phases. Squares represent values calculated for alloy 4 ($\bar{m} = 2.5$).

Fig. 7 Measured values of $a_{10}$ (copper-poor phase) and $a_{20}$ (copper-rich phase) as a function of temperature are designated by squares and solid lines. Values of $a_{10}$ and $a_{20}$ calculated from tetragonal data are given by circles and dashed lines.

TABLE I. Compositions of alloys 1-4 with volume fractions $f_1$ and $f_2$ determined from the phase diagram. Copper-poor phase is indicated by subscript one.

| Alloy | Cu | Ni | Fe | $f_1$ | $f_2$ |
|---|---|---|---|---|---|
| 1 | 54.4 | 36.7 | 8.9 | .25 | .75 |
| 2 | 41.8 | 44.8 | 13.4 | .50 | .50 |
| 3 | 30.7 | 52.5 | 16.8 | .68 | .32 |
| 4 | 50 | 35 | 15 | .43 | .57 |

TABLE II. Measured and calculated yield stresses for alloys 1-3. Calculated values in the columns with $\bar{m} = 3.06$ and $\bar{m} = 2.75$ are respectively for samples with randomly oriented grains and for samples that have a preferred orientation of grains caused by fabrication.

| Alloy | Aging Temp. | Measured Yield Stress | Calculated Yield Stresses | |
|---|---|---|---|---|
| | | | $\bar{m} = 3.06$ | $\bar{m} = 2.75$ |
| 1 | 625°C | 47,150 psi | 54,550 psi | 49,100 psi |
| 2 | 625°C | 47,150 | 52,270 | 47,040 |
| 3 | 625°C | 48,030 | 50,740 | 45,670 |
| 1 | 450°C | 63,820 | 71,280 | 64,640 |
| 2 | 450°C | 63,050 | 68,760 | 61,880 |
| 3 | 450°C | 62,900 | 66,700 | 60,030 |

TABLE III. Measured and calculated yield stresses for alloy 4. Calculated values in the columns with $\bar{m} = 3.06$ and $\bar{m} = 2.5$ are respectively for samples with randomly oriented grains and for samples that have a preferred orientation of grains caused by fabrication.

| Alloy | Aging Temp. | Measured Yield Stress | Calculated Yield Stresses $\bar{m} = 3.06$ | $\bar{m} = 2.5$ |
|---|---|---|---|---|
| 4 | 800°C | 29,500 psi | 39,770 psi | 32,490 psi |
| 4 | 730°C | 40,900 | 50,330 | 41,120 |
| 4 | 625°C | 53,620 | 64,880 | 52,940 |
| 4 | 550°C | 62,290 | 76,220 | 62,270 |

TABLE IV. Elastic modulus and compliance data and estimates used to compute yield strengths of aged Cu-Ni-Fe alloys. References are given by lower case latters. Data on lines 3 and 4 were used for yield strength calculations of alloys 1-3, lines 5 and 6 were used with alloy 4.

| Line | Material | Young's Modulus $10^6$ psi | Elastic Compliances $10^{-12}$ cm$^2$/dyne $S_{11}$ | $S_{12}$ | $S_{44}$ | $S_{11} + S_{12}$ |
|---|---|---|---|---|---|---|
| 1 | Nickel | 30[a] | .80 | -.31 | 0.84[d] | .49 |
| 2 | Copper | 17[b] | 1.49 | -.63 | 1.3[d] | .86 |
| 3 | 65Ni-35Fe | 26[a] | .923 | -.358 | | .565 |
| 4 | 70Cu-30Ni | 22[c] | 1.150 | -.485 | | .665 |
| 5 | 60Ni-40Fe | 25[a] | .960 | -.370 | | .590 |
| 6 | 80Cu-20Ni | 21 est. | 1.205 | -.510 | | .695 |

a) Taylor, L., Editor, Metals Handbook (American Society for Metals, Cleveland, Ohio, 1948) p.600.

b) Ibid., p. 906.

c) Ibid., p. 925.

d) Mason, Warren P., Physical Acoustics and the Properties of Solids (D. Van Nostrand Co., Inc., Princeton, N. J. 1958) p. 358.

TABLE V. Equilibrium cubic lattice parameters determined from references 1 and 2 for alloys 1-3 and measured for alloy 4. Equation (18) was used to determine $\bar{a}$.

| Alloy | Aging Temp. | Cu-Poor Phase $a_{10}$ | Cu-Rich Phase $a_{20}$ | $\Delta a_o$ | Calculated $\bar{a}$ |
|---|---|---|---|---|---|
| 1 | 625°C | 3.558 kx | 3.577 kx | .019 kx | 3.572 kx |
| 2 | 625°C | 3.558 | 3.577 | | 3.567 |
| 3 | 625°C | 3.558 | 3.577 | | 3.563 |
| 1 | 450°C | 3.555 | 3.580 | .025 | 3.573 |
| 2 | 450°C | 3.555 | 3.580 | | 3.566 |
| 3 | 450°C | 3.555 | 3.580 | | 3.562 |
| 4 | 800°C | 3.579Å | 3.594Å | .015Å | 3.587Å |
| 4 | 730°C | 3.574 | 3.597 | .023 | 3.586 |
| 4 | 625°C | 3.570 | 3.600 | .030 | 3.585 |

TABLE VI. Tetragonal data from Hargreaves[7] used to determine the cubic parameters of the precipitating phases. Values indicated by asterisks were determined from the graph in Fig. 7. Equation (22) was used to determine $a_{10}$ and $a_{20}$.

| Aging Temp. | $\bar{a}$ | Cu-Poor Phase $c_1/\bar{a}$ | Cu-Rich Phase $c_2/\bar{a}$ | Calculated Values | | |
|---|---|---|---|---|---|---|
| | | | | $a_{10}$ | $a_{20}$ | $\Delta a_o$ |
| 800°C | 3.586Å | .995 | 1.005 | 3.578Å | 3.593Å | .015Å |
| 730°C* | 3.586 | | | 3.576 | 3.595 | .019 |
| 650°C | 3.586 | .993 | 1.008 | 3.575 | 3.598 | .023 |
| 625°C* | 3.586 | | | $3.573_7$ | $3.598_3$ | .025 |
| 550°C | 3.586 | .991 | 1.010 | 3.572 | 3.601 | .029 |

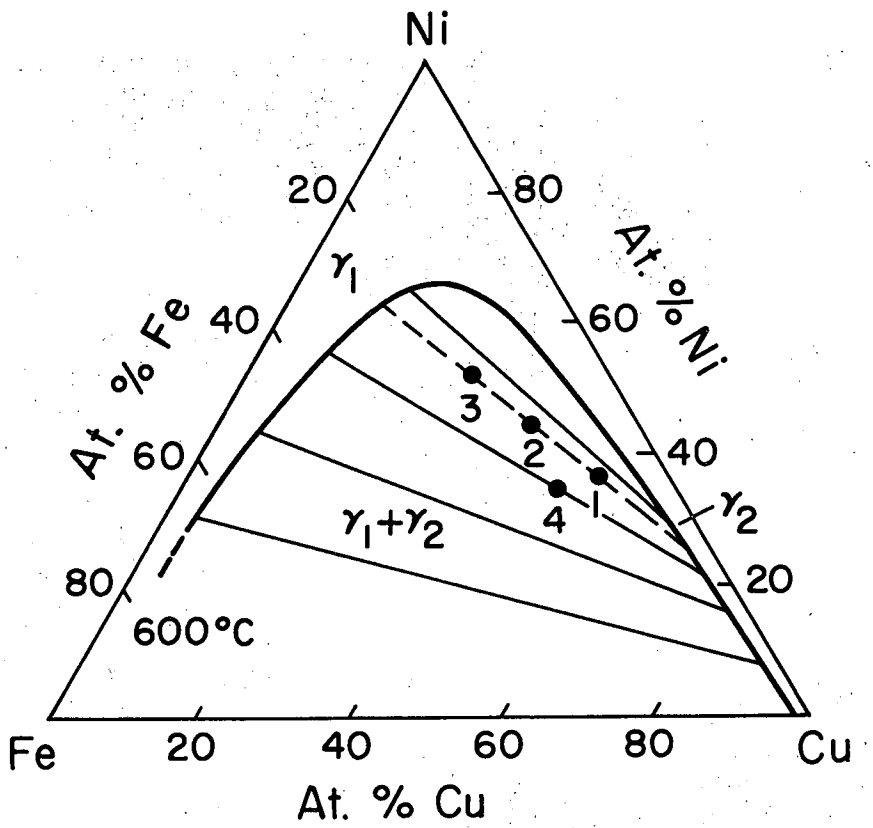


MUB-9676

Fig. 1

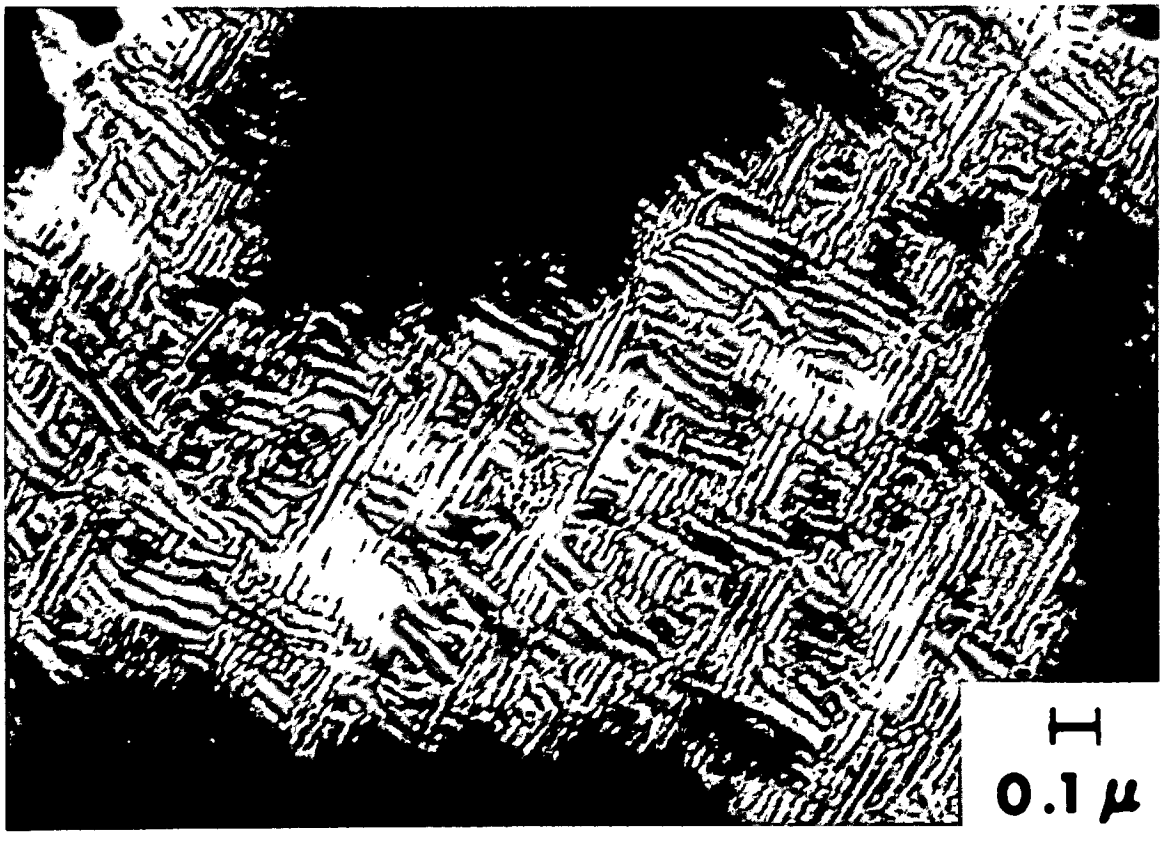


ZN-5498

Fig. 2

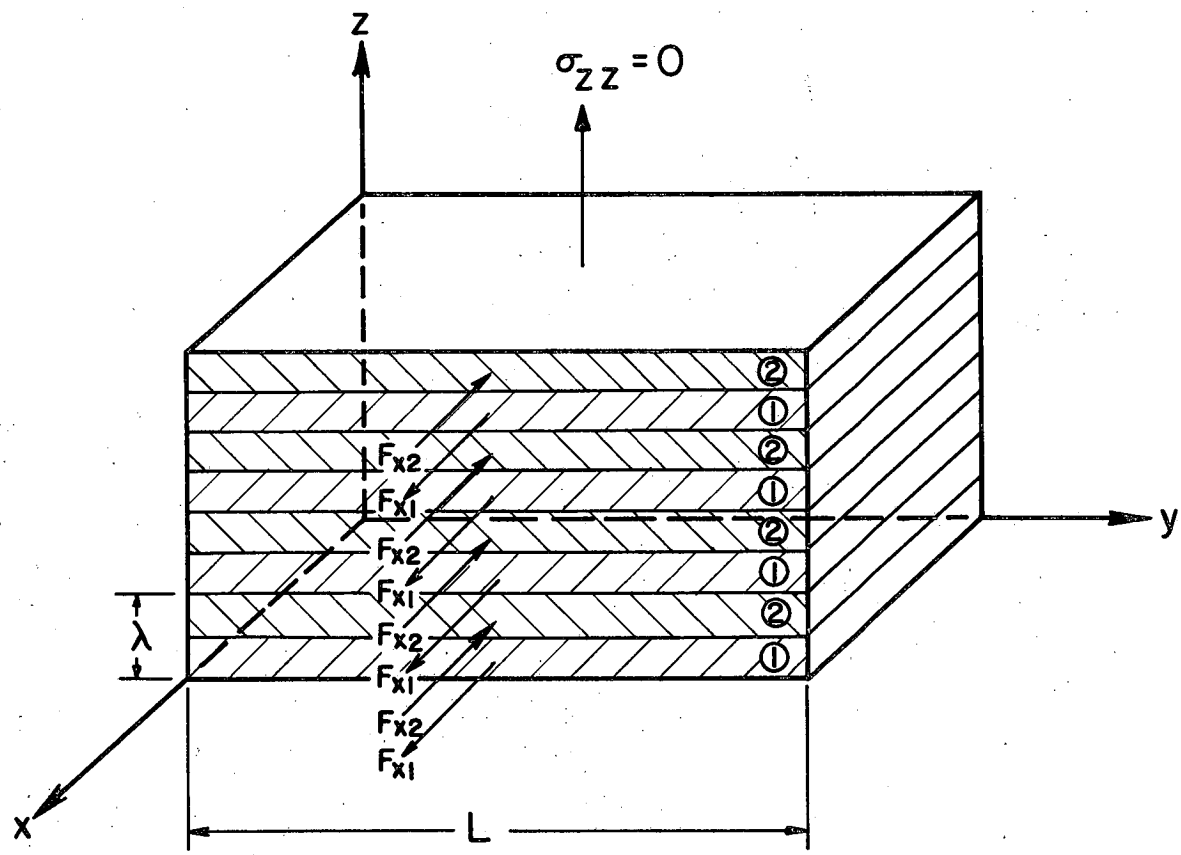


MUB-9674

Fig. 3

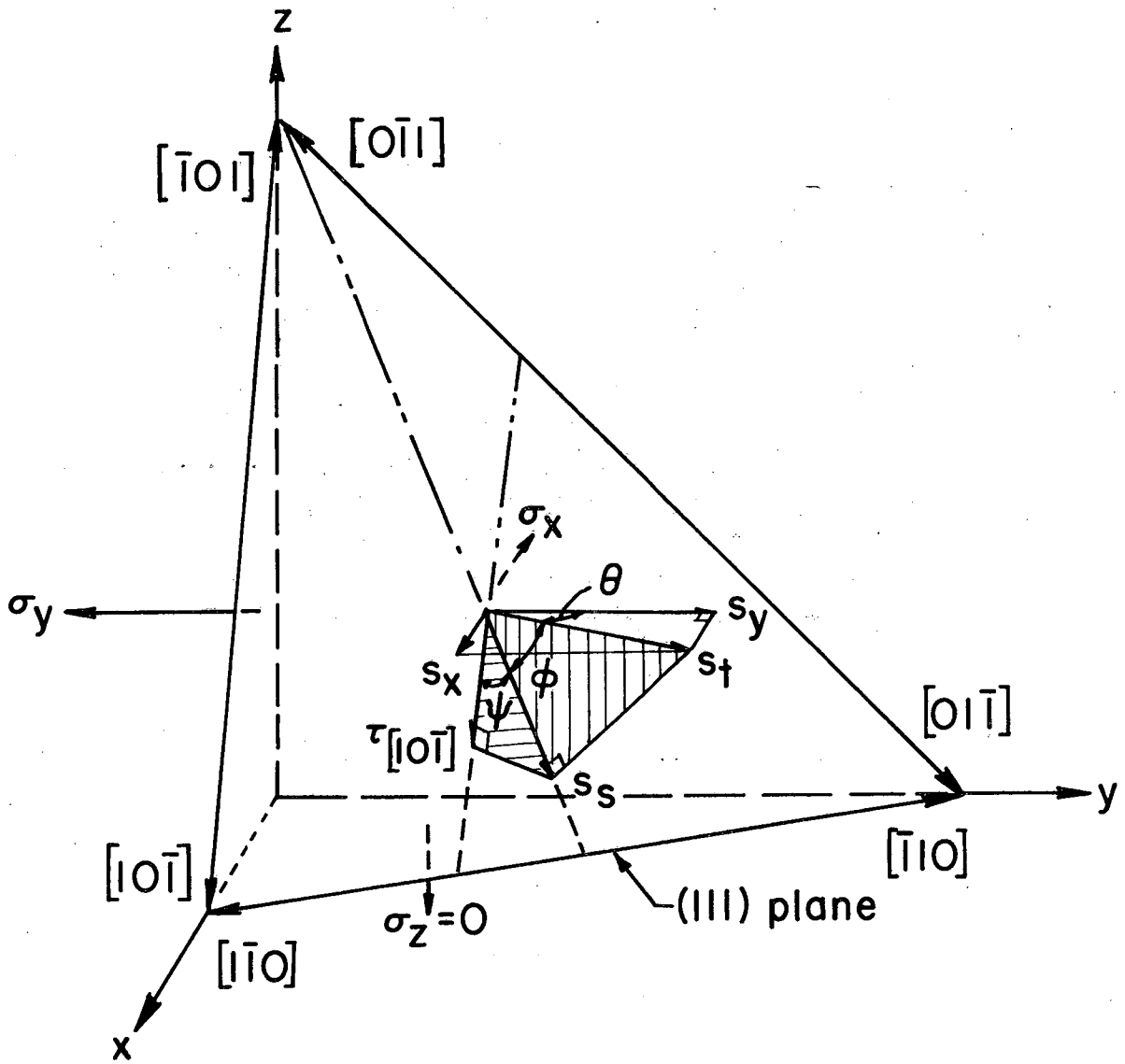


MUB-9673

Fig. 4

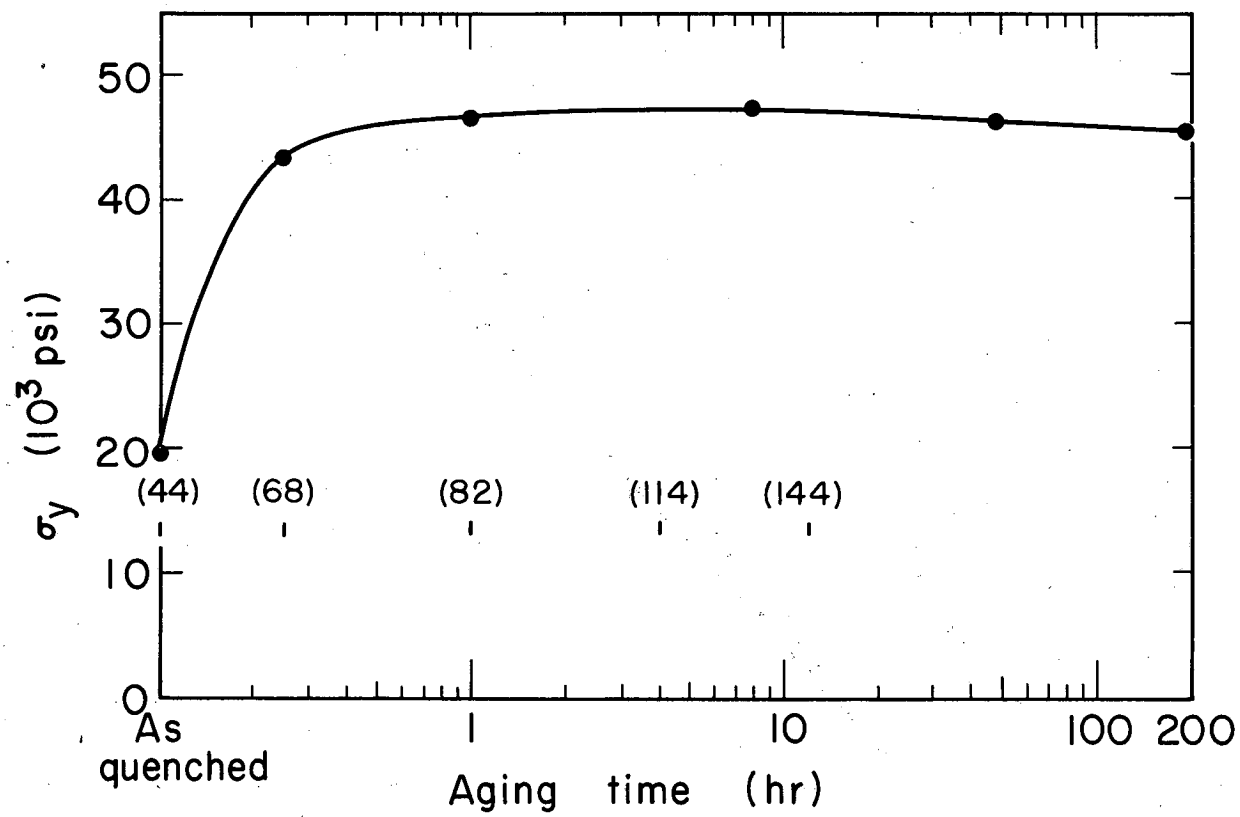


MUB-9675

Fig. 5

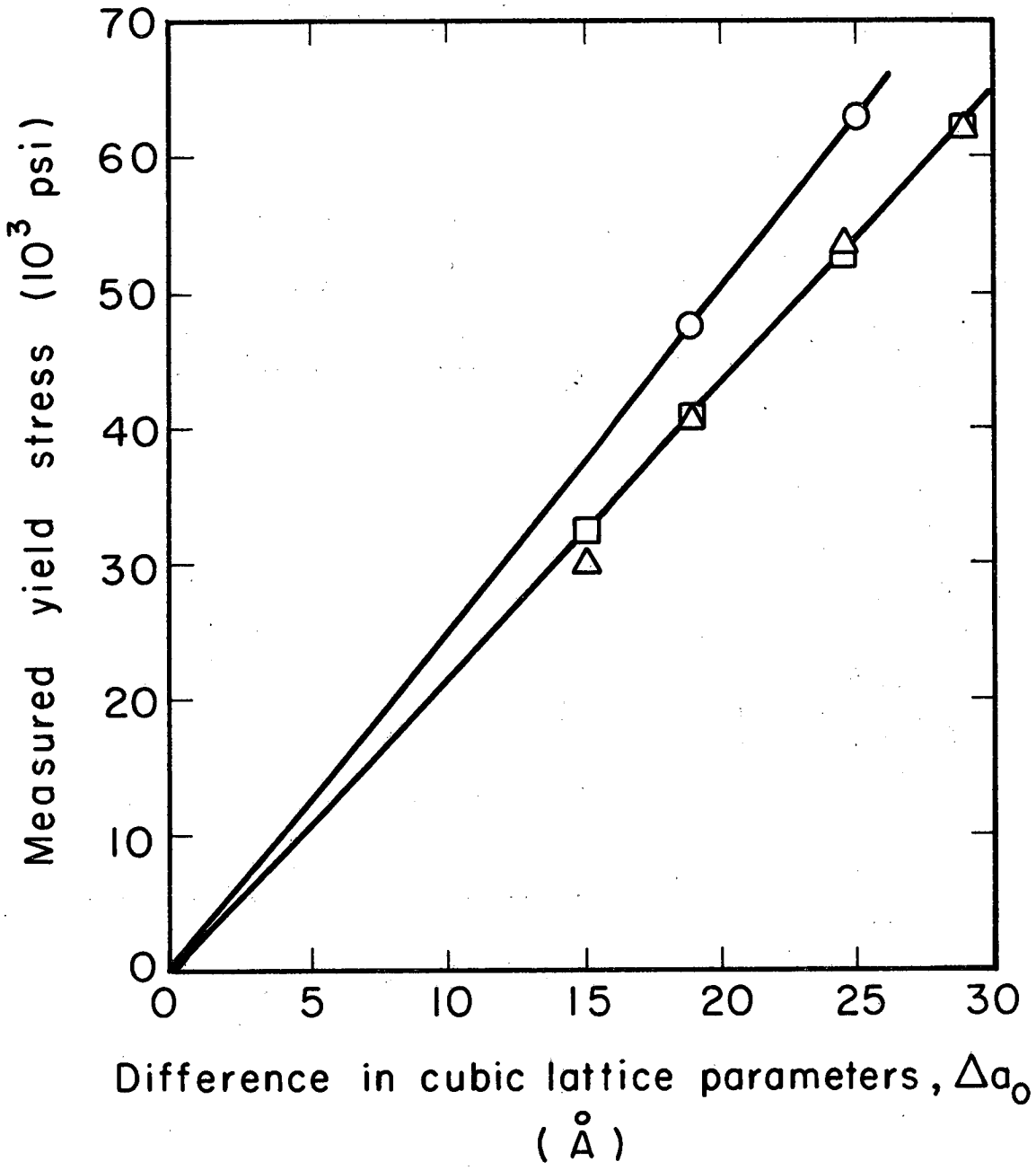


MUB-10538

Fig. 6

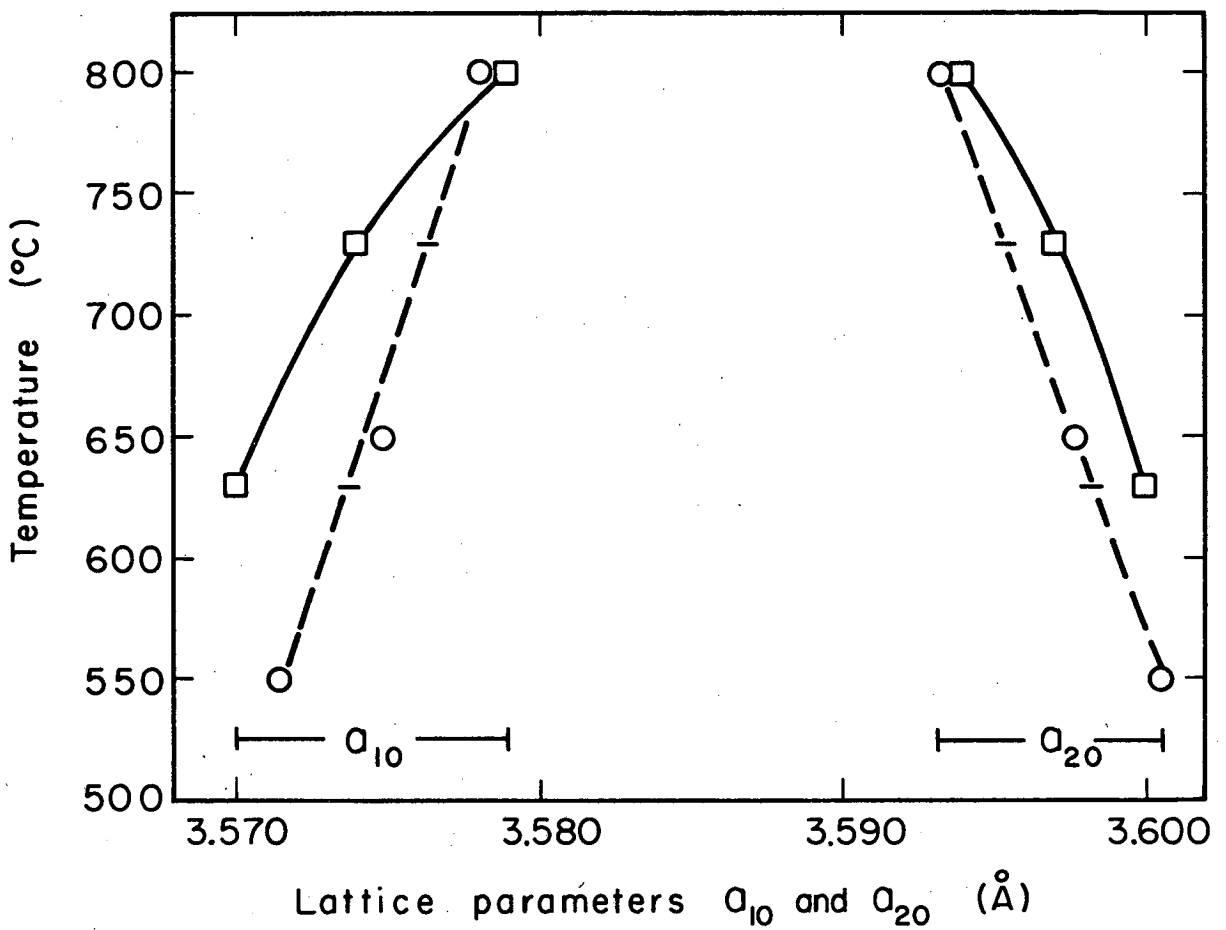


MUB-10537

Fig. 7

This report was prepared as an account of Government sponsored work. Neither the United States, nor the Commission, nor any person acting on behalf of the Commission:

A. Makes any warranty or representation, expressed or implied, with respect to the accuracy, completeness, or usefulness of the information contained in this report, or that the use of any information, apparatus, method, or process disclosed in this report may not infringe privately owned rights; or

B. Assumes any liabilities with respect to the use of, or for damages resulting from the use of any information, apparatus, method, or process disclosed in this report.

As used in the above, "person acting on behalf of the Commission" includes any employee or contractor of the Commission, or employee of such contractor, to the extent that such employee or contractor of the Commission, or employee of such contractor prepares, disseminates, or provides access to, any information pursuant to his employment or contract with the Commission, or his employment with such contractor.